Magnetic and electronic phase separation driven by structural clustering in $La_{0.7}(Ca_{1−y}Sr_y)_{0.3}MnO_3$ thin films

V.G. Prokhorov, V.A. Komashko, and G.G. Kaminsky

Institute of Metal Physics of the National Academy of Sciences of Ukraine, Kiev 03142, Ukraine
E-mail: pvg@imp.kiev.ua

Y.P. Lee, Y.H. Hyun, K.K. Yu, and J.S. Park

q-PSI and Department of Physics, Hanyang University, Seoul 133-791, Korea

V.L. Svetchnikov

National Center for HREM, TU Delft 2628AL, The Netherlands

The structural, magnetic and transport properties of $La_{0.7}(Ca_{1−y}Sr_y)_{0.3}MnO_3$ films deposited on $LaAlO_3$ (001) single-crystalline substrate by rf-magnetron sputtering using «soft» (or powder) targets are investigated. It was found that at $0.3 \leq y \leq 0.5$ both rhombohedral ($\overline{R}3c$) and orthorhombic ($Pnma$) crystal phases are coexistent at room temperature, forming a nanoclustered microstructure. The clustered films manifest the two-stage magnetic and electronic transition, which are typical for the phase-separated systems. It was shown that for $0.5 \geq y \geq 0$ the nonlinear (almost parabolic) field-dependent magnetoresistance is typical at room temperature while for $0.65 \leq y \leq 1.0$ its transform to the linear behavior. The magnetotransport properties of the films are explained within the framework of a field-dependent activation energy model. The magnetic phase diagram for the $La_{0.7}(Ca_{1−y}Sr_y)_{0.3}MnO_3$ thin-film system is presented.

1. Introduction

The discovery of a huge negative magnetoresistive effect in doped manganite perovskites with the general formula $R_{1−x}A_xMnO_3$, where R is a rare-earth cation and A is alkali or alkaline earth cation [1], called «colossal magnetoresistance» (CMR), attracted interest to these compounds [2−5]. The transport and magnetic properties of doped manganites can be understood within the framework of «double exchange» (DE) model which considers the magnetic coupling between Mn^{3+} and Mn^{4+} that results from the motion of an itinerant electron between two partially filled d shells with strong on-site Hund's coupling [6−8], and taking into account Jahn−Teller spin- and charge−lattice interactions [9,10]. At the same time, because the hole-doped perovskite manganites belong to the strongly correlated systems, they manifest a tendency toward a phase separation, typically involving the ferromagnetic (FM) metallic and charge-ordered insulating domains [11]. Such type of the phase-separated state usually occurs in a temperature range below the Curie point (T_C). On the other hand, the nanoscale structural correlations were observed recently in the $La_{0.65}(Ca_{0.45}Sr_{0.55})_{0.35}MnO_3$ single crystal at the temperature more above T_C [12]. The main reason of this effect is the trend of $La_{0.7}(Ca_{1−y}Sr_y)_{0.3}MnO_3$ to the structural transition from the rhombohedral ($\overline{R}3c$) to orthorhombic ($Pnma$) crystal lattice with decreasing temperature near $y \simeq 0.5$ [13−17]. Moreover, this transition is controlled by an external magnetic field, indicating a small difference between the ground state energies for these crystal symmetries [15]. At the same time, the overwhelming majority of these data were observed on

the bulk materials which undergo the structural transition under equilibrium thermodynamic conditions. It is reasonable to suggest that a strong influence of the substrate on the crystal lattice of deposited film should be result in the structural modification of this compound.

In this paper we report on the magnetotransport properties of the as-deposited $La_{0.7}(Ca_{1-y}Sr_y)_{0.3}MnO_3$ films at fixed the Mn^{3+}/Mn^{4+} ratio for varying size of the dopant atoms. It was shown that the $0.3 \leq y \leq 0.5$ films manifest the multiple microstructure which contains the nanoscale clusters of both the orthorhombic and the rhombohedral crystal lattice at room temperature. We find that films with $0.5 \geq y \geq 0$ demonstrate a nonlinear (almost parabolic) behavior of the magnetoresistance (MR) versus an applied magnetic field while for $0.65 \leq y \leq 1.0$ the MR(H) has almost a linear one at room temperature. This effect is described within the framework of a field-affected activation energy approximation, taking into account a competition between the spin-dependent trapping of charges and the Weiss-magnetization contribution. Using experimental data, the magnetic phase diagram is constructed for the $La_{0.7}(Ca_{1-y}Sr_y)_{0.3}MnO_3$ thin-film system.

2. Experimental Techniques

The films were prepared by on-axis rf-magnetron sputtering using the so-called «soft» (or powder) target [18]. The substrate was a $LaAlO_3$ (LAO) single crystal with an out-of-plane lattice parameter $c \simeq 0.379$ nm for a pseudocubic symmetry. The total pressure in chamber was $4 \cdot 10^{-2}$ Torr with a gas mixture of Ar and O_2 (2 : 1). The substrate temperature during deposition was 750° C. Under these conditions $La_{0.7}(Ca_{1-y}Sr_y)_{0.3}MnO_3$ films with $y = 1.0, 0.9, 0.8, 0.65, 0.5, 0.3,$ and 0 were prepared. The thickness of all the films was $d \simeq 100$ nm. The θ−2θ x-ray diffraction (XRD) patterns were obtained using a Rigaku diffractometer with Cu-K_α radiation. High-resolution electron-microscopy (HREM) studies were carried out using a Philips CM300UT-FEG microscope with a field emission gun operated at 300 kV. The point resolution of the microscope was of the order of 0.12 nm. The cross-sectional specimens were prepared by the standard techniques using mechanical polishing followed by ion-beam milling at a grazing incidence. All microstructure studies were carried out at a room temperature. The resistance measurements were performed by using the four-probe method in a temperature range of 4.2−300 K and a magnetic field up to 5 T. The in-plane field-cooled (FC) and the zero-field-cooled (ZFC) magnetization curves in a field of 100 Oe and the magnetization hysteresis loops at 10 K were taken with a Quantum Design SQUID magnetometer.

3. Microstructures of the films

The analysis of the θ−2θ XRD scans (not shown) manifests that the deposition results in highly c-oriented films without the traces of parasitic phases. Figure 1 shows, in detail, the (004) Bragg peak for all $La_{0.7}(Ca_{1-y}Sr_y)_{0.3}MnO_3$ films. It is seen that the substitution of Sr by Ca shifts, from the beginning, the Bragg peak to high-angle side while at $y \lesssim 0.5$ the opposite tendency is observed. Therefore, the out-of-plane lattice parameter nonmonotonically depend on y in contrast to the expected behavior for bulk. It is clear that reduction in Sr doping should be lead to a monotonic decrease in the lattice parameter because the Ca ion radius is smaller than that of the Sr one. The observed nonmonotonic behavior of c can be explained by the more expressive tendency of the $La_{0.7}Ca_{0.3}MnO_3$ film to accumulation of the lattice strain, during epitaxial growth, than that observed for the $La_{0.7}Sr_{0.3}MnO_3$ one [19−21].

For illustration of this fact Fig. 2 exhibits the high-magnification cross-sectional HREM images of the $La_{0.7}Ca_{0.3}MnO_3$ (*a*) and the $La_{0.7}Sr_{0.3}MnO_3$ (*b*) films for regions including the interface between film and substrate (denoted by white dashed line). Insets (A) are the corresponding fast Fourier transform (FFT) of these HREM images. It is seen that the FFT
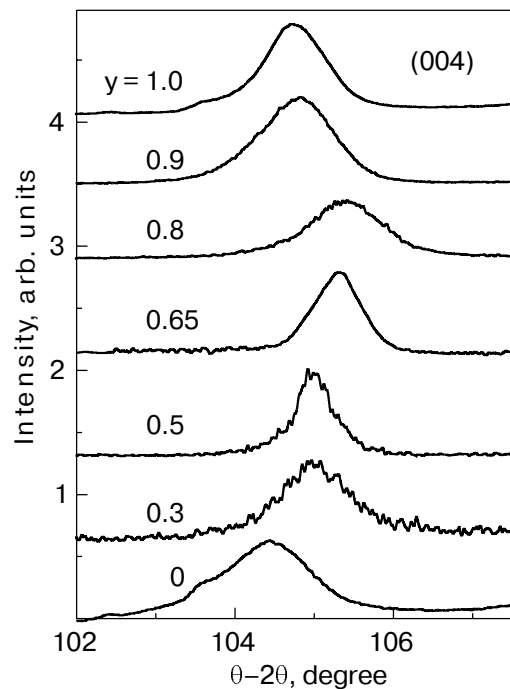

Fig. 1. XRD patterns in the vicinity of the (004) Bragg peak for the $La_{0.7}(Ca_{1-y}Sr_y)_{0.3}MnO_3$ films.

pattern of the $La_{0.7}Sr_{0.3}MnO_3/LAO$ interface reveals elongated and slightly-split spots in both c (normal to the interface) and a (along the interface) directions (indicated by white arrows). This is an evidence for a semicoherent (or weaklycoherent) lattice coupling between the film and the substrate. In contrast to that FFT for the $La_{0.7}Ca_{0.3}MnO_3/LAO$ interface produces a rectangular pattern with a well-defined spot splitting in the out-of-plane direction only, manifesting a nearly coherent interface between the film and the substrate. It is confirmed by the moire patterns (or inverse Fourier transforms [22]), which are represented by the insets (B) in Figs. 2,a,b. It is seen that the edge misfit dislocation occurs in the $La_{0.7}Sr_{0.3}$ MnO_3 film while it is not observed in the $La_{0.7}Ca_{0.3}MnO_3$ one. The measurement of various interspot spacings on the high-magnification HREM image allows us to obtain the average values of lattice parameters. Analysis reveals that both films have a tetragonal distortion
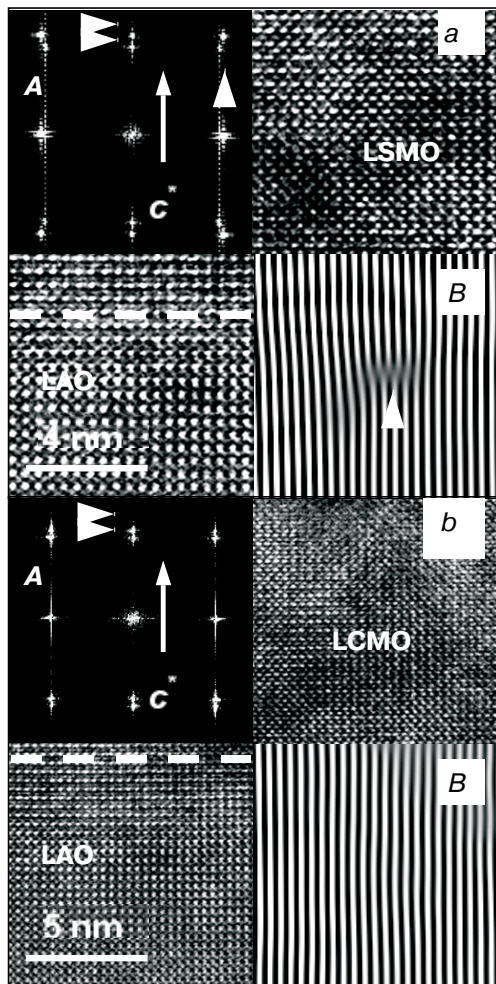
of the crystal lattice $c/a \simeq 1.01$ and 1.02 for $La_{0.7}Sr_{0.3}MnO_3$ and $La_{0.7}Ca_{0.3}MnO_3$, respectively, where a is an in-plane lattice parameter. Therefore, the observed increasing in the out-of-plane lattice parameter in the Ca-rich ($y \le 0.5$) films is provided by an intensive tetragonal distortion owing to formation of a coherent interface between the film and the substrate. Figure 3 shows the high-magnification cross-sectional HREM images of $La_{0.7}(Ca_{1-y}Sr_y)_{0.3}MnO_3$ for $y = = 0.5$ (a) and 0.65 (b), respectively. The $y = 0.5$ film contains areas with more or less different crystal structure, the boundaries of which are marked by white dashed lines. It is coincident with the FFT pattern which exhibits that the main spots are elongated in the out-of-plane direction, confirming a variety of the lattice parameters. Moreover, the additional slight spots (correspondent to the doubled lattice parameter) are distinguishable on the FFT pattern (denoted by white arrow) in zones with a violent atomic ordering. Similar zone in the real space is indicated by white arrow in Fig. 3,a. Figure 3,c shows the Fourier filtration of the original HREM image, which allows us to distinguish the areas with different atomic ordering more accurately. These areas, corresponding to dark and bright regions in Fig. 3,c, have a size from few a nanometers to tens of nanometers. The measurement of a large number of interdot spacings and angles between dot rows allow us to obtain the average lattice parameters for both crystalline phases. Upon analysis, one can conclude that the more-ordered zones manifest a rhombohedral crystal structure with $a_R \simeq 0.5484$ nm and $\alpha_R \simeq 60.35°$ while, the more-dis-
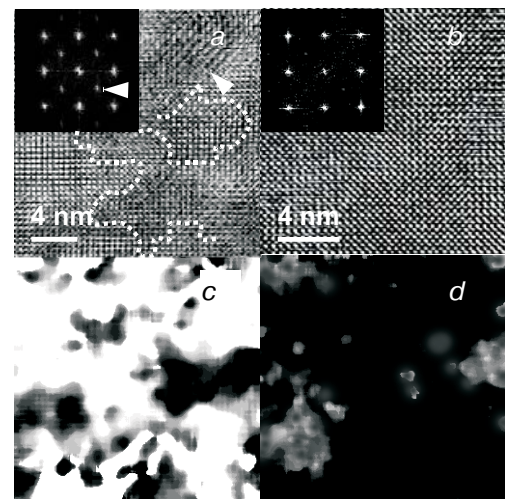

Fig. 2. High-magnefication cross-sectional HREM images for the $La_{0.7}Sr_{0.3}MnO_3$ (a) and $La_{0.7}Ca_{0.3}MnO_3$ (b) films. Dashed lines indicate the film/substrate interface. Insets (A) are corresponding FFT. Insets (B) show corresponding moire patterns.

Fig. 3. (a) and (b) cross-sectional HREM images for the $La_{0.7}(Ca_{1-y}Sr_y)_{0.3}MnO_3$ film with $y = 0.5$ and 0.65, respectively. Insets are the FFT of corresponding HREM images. (c) and (d) Fourier filtration of the (a) and (b) original HREM images. Dashed lines in (a) indicate regions with different crystal structure.

ordered ones have an orthorhombic crystal lattice with tetragonal ratio of $c/a \simeq 1.02$ and $a \simeq 0.3812$ nm. Therefore, the $La_{0.7}(Ca_{1-y}Sr_y)_{0.3}MnO_3$ film at $y = 0.5$ can be treated as a composite object which involves two kinds of the nanoscale clusters with a different crystal lattice. The observed contradiction with the XRD data, which manifest only a single unsplit Bragg peak, can be explained by the similarity of the lattice parameters (for a pseudocubic symmetry) for the both crystal structures and the detection limit of the x-ray diffraction with Cu-K_α radiation. However, it should be noted that structural clustering was observed recently by a powder XRD measurement near the (022, 220) reflection in the corresponding bulk compound [17]. For comparison, Fig. 3,*b* shows that the film at $y = 0.65$ manifests an almost uniform crystal lattice. Inset in Fig. 3,*b* displays that FFT produces a rectangular pattern of circular and non-elongated spots, and Fig. 3,*d* represents the more monotonous contrast of the Fourier filtration than that observed for $y = 0.5$. Analysis reveals that this film has mainly a rhombohedral crystal structure with $a_R \simeq 0.5524$ nm and $\alpha_R \simeq 60.46°$, which are coincident with the bulk [15].

4. Magnetic and transport properties

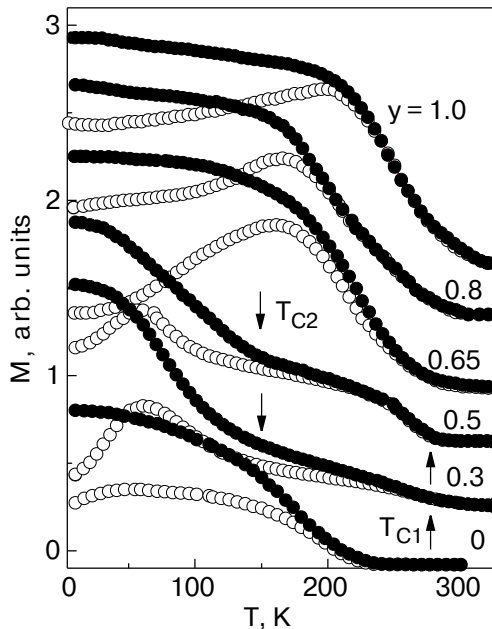Figure 4 shows the in-plane FC (solid symbols) and ZFC (open symbols) temperature-dependent magnetization curves, $M(T)$, for $y = 1.0, 0.8, 0.65, 0.5, 0.3,$ and 0. The applied magnetic field was $H = 100$ Oe. It is seen that an increase in the substitution of Sr by Ca leads to a gradual decrease of T_C, except for the $y = 0.5$ and 0.3 films. For these films $M(T)$ manifests behavior typical for a two-phase magnetic system. A first transition occurs at $T_{C1} \simeq 260$ K and second one at $T_{C2} \lesssim 130$ K, as a slight change in the slope of the FC curve. It worthy of note that similar two-step $M(T)$ behavior was observed recently in a single crystal at $y = 0.45$ and explained by the occurrence of a structural transition at temperature below T_C [16]. However, according to the microstructural analysis for $y = 0.5$, in our case we are dealing with a composite film which involves two kinds of nanoscale clusters with a different crystal lattice. Therefore, it is reasonable to suggest that the two-stage $M(T)$ dependence is a simple superposition of two separated FM transitions in clusters with the rhombohedral and orthorhombic structure. At the same time, the $y = 0.3$ film also demonstrates the two-step $M(T)$ behavior and can be treated as a crystal-phase-separated system as well, though the FM response at T_{C1} is significantly suppressed in comparison with $y = 0.5$.

Figure 5 shows the temperature-dependent resistance, $R(T)$, for the same films without (solid symbols) and with (open symbols) an applied magnetic field of 5 T. The magnetic field was directed parallel to the film surface and at right angle to the transport

Fig. 4. Temperature dependence of the FC (solid symbols) and ZFC (open symbols) magnetizations for the $La_{0.7}(Ca_{1-y}Sr_y)_{0.3}MnO_3$ films. Arrows indicate the Curie point for the magnetic phase-separated films.
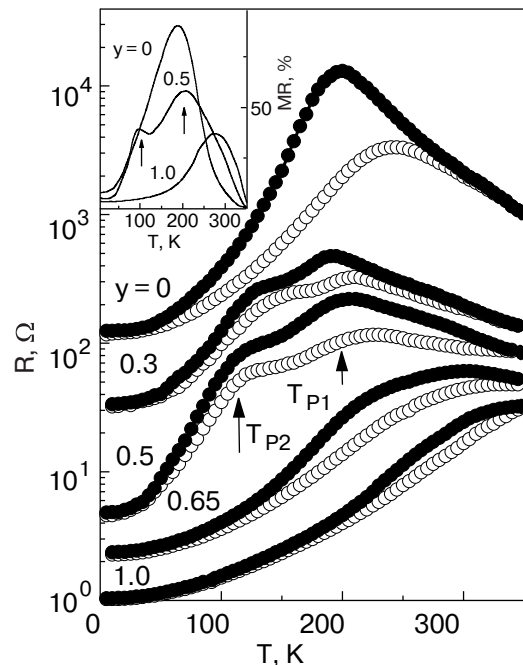

Fig. 5. Temperature dependence of the resistance for the $La_{0.7}(Ca_{1-y}Sr_y)_{0.3}MnO_3$ films without (solid symbols) and with (open symbols) an applied magnetic field of 5 T. Arrows indicate the two-stage MI transition in the $y = 0.5$ and 0.3 films.

current. It is seen that the $y = 0$ film demonstrates a typical CMR $R(T)$ behavior with the well-defined metal−insulator (MI) transition at $T_P \simeq$ 200 K, while the $y = 1.0$ one manifests only a change in the slope on the $R(T)$ dependence at $T \simeq$ 300 K. It is known that the $La_{0.7}Sr_{0.3}MnO_3$ compound, owing to a large one-electron bandwidth, does not undergo a real MI transition near Curie point and retain a metal-like state in the paramagnetic phase up to high temperatures [5,15]. On the other hand, the $y = 0.3$ and 0.5 films demonstrate two-peak behavior of $R(T)$, which can be treated as two MI transitions at $T_{P1} \lesssim$ 210 K and $T_{P2} \lesssim$ 130 K (indicated by arrows), which are governed by the appearance of FM ordering in the rhombohedral and orthorhombic clusters, respectively. It is confirmed by the similar two-peak temperature behavior of MR for $y = 0.5$, which is shown in the inset. Moreover, these peaks occur at temperatures close to T_{P1} and T_{P2} on the $R(T)$ curve. Here the MR value is defined by $100\% \times [R(0) - R(H)]/R(0)$, where $R(0)$ and $R(H)$ are the resistances without and with a magnetic field of 5 T, respectively.

Figure 6 displays the magnetic-field dependence of MR at room temperature for the $y = 0.3, 0.5, 0.8,$ and 0.9 films. In this case the MR value is defined by $100\% \times [R(H) - R(0)]/R(0)$. It is seen that a magnetoresistive effect is enhanced with increasing Sr doping, and the MR(H) dependence is changed from almost parabolic ($y = 0.3$ and 0.5) to close to linear ($y = 0.8$ and 0.9). A similar variation of the MR(H) behavior at $T \geq T_C$ has already been observed in these lanthanides and explained by a transition from the in-

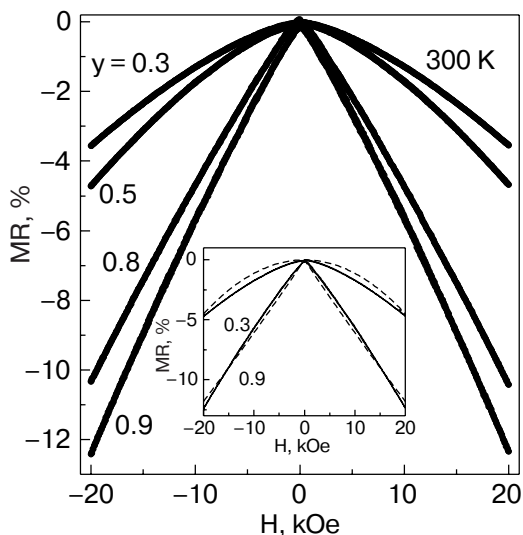sulating to metal-like state with increasing of Sr concentration [23−26]. However, in these publications the opposite dependence of a magnetoresistive effect on the Sr doping was observed [15,26].

5. Discussion

Figure 7 exhibits a magnetic phase diagram for the $La_{0.7}(Ca_{1-y}Sr_y)_{0.3}MnO_3$ films deposited on the LAO substrate. The triangular symbols display a temperature T_P of the MI transition. It is seen that the decrease of Sr doping, in general, leads to decrease of T_C, which is coincident with published results for bulk [15] and thin films deposited on $NdGaO_3$ [26]. Because the FM ordering is governed by the transfer interaction of an e_g-orbital carrier between the neighboring Mn sites, which should be determined mainly by Mn−O bond length and Mn−O−Mn angle [23], the final result for T_C can be approximately written as [27,28] $T_C \sim W \sim \cos\varphi / d_{Mn-O}^{3.5}$, where W is the bandwidth, φ is the tilt angle in the plane of the bond, and d_{Mn-O} is the Mn−O bond length. Consequently, the modification of a crystal lattice from rhombohedral to orthorhombic owing to a substitution of Sr for Ca, which usually is accompanied by the decreasing tilt angle, must lead to the W narrowing and the T_C decreasing. It is believable that the parent $La_{0.7}Sr_{0.3}MnO_3$ compound has a rhombohedral crystal structure with $\varphi \approx 165°$, while $La_{0.7}Ca_{0.3}MnO_3$ has a orthorhombic one with $\varphi \approx 155°$. However, in contrast to bulk which shows the structural $\overline{R}3c \rightarrow Pnma$ transition at a certain y concentration [15], our films manifest the suffi-

Fig. 6. Magnetic-field dependence of MR ratio for the $La_{0.7}(Ca_{1-y}Sr_y)_{0.3}MnO_3$ films measured at room temperature. Inset displays the experimental (solid lines) and theoretical (dashed lines) MR(H) dependence for the $y = 0.3$ and 0.9 films.

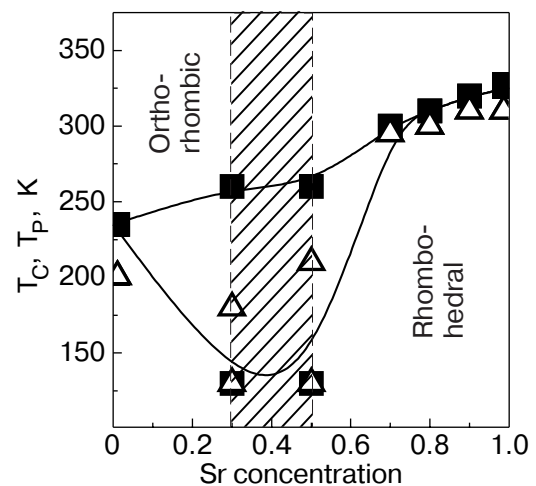*Fig. 7.* Magnetic phase diagram for the $La_{0.7}(Ca_{1-y}Sr_y)_{0.3}MnO_3$ thin-film system. Solid squares and open triangles correspond to the Curie point and the temperature of the MI transition. The concentration range of the structural phase-separated state is crosshatched.

ciently broad concentration range $(0.3 \leq y \leq 0.5)$ where both crystalline phases are coexistent. It was declared above, the observed multiple clustering in these films probably is governed by a nonuniform distribution of the lattice strain. Consequently, for the $0.3 \leq y \leq 0.5$ films, it is reasonable to suggest that with temperature decreasing the FM phase appears at first in the rhombohedral clusters and then in the orthorhombic regions of the film, providing the two-stage $M(T)$ behavior. The small magnetization raising at T_{C1} for the $y = 0.3$ film (see curve *6* in Fig. 4) can be explained by the decrease in an amount of clusters with the rhombohedral structure with the increasing Ca doping. Analysis of Figs. 4 and 5 displays that the magnetic and electronic transition temperatures $(T_{C2} \simeq T_{P2} \simeq 130$ K$)$ are almost coincident for the orthorhombic regions of the $y = 0.3$ and 0.5 films which testify to the typical MI transition resulted from the DE mechanism [5]. At the same time a significant discrepancy between the FM and MI transition temperatures is observed for the rhombohedral clusters: $T_{C1} \simeq 260$ K against $T_{P1} \simeq 180$ and 210 K for $y = 0.3$ and 0.5, respectively. This divergence can be explained by a percolating mechanism of the MI transition, which is very often observed in the inhomogeneous manganites independently of the physical nature of this inhomogeneity [11].

Let us consider a field-dependent magnetoresistance behavior of the films at room temperature. According to the phase diagram the films with large Sr doping $(y \geq 0.65)$ manifest an onset of the FM transition at $T \gtrsim 300$ K. Therefore, MR(H) should be obey the DE mechanism of the charge transport, which predicts a square dependence on magnetization: MR$(H) = C(M/M_s)^2$ [2,29]. Here M_s is the saturation magnetization and C is a nearly field- and temperature-independent constant. On the other hand, the films with lager Ca doping $(y \leq 0.5)$ have the Curie point below a room temperature and at $T > T_C$ demonstrate the thermally activated polaronic transport of carriers (see Fig. 5), expressed by $R(T,H) = R_0 T \exp(E_A/k_B T)$. Here R_0 is the constant, which is inversely proportional to the polaron hopping frequency, E_A is the activation energy, and k_B is the Boltzmann constant. Consequently, the $y \leq 0.5$ films can be treated as paramagnetic insulators at room temperature. The MR(H) behavior of such materials is explained as a rule by two approaches. The first of them is based on the idea that the hopping probability of the insulator with a short-range magnetic ordering should be modified by a multiplicative term $(1 + M^2/M_s^2)/2$ [30]. In this case the negative magnetoresistance ratio also has the square dependence on a magnetization with $C = 1$ and expressed by MR$(H) = (M/M_s)^2$. The se-

cond approach assumes that the trapping of a charge (treated as a ferromagnetic polaron) can be minimized by the transition of the paramagnetic neighborhood from random disorder to spin alignment due to an applied magnetic field [25,31]. In this case the activation energy has to change in the presence of a magnetic field, $E_A = E_A^0(1 - \langle \cos \theta_{ij} \rangle)$, where E_A^0 is the field-independent activation energy and θ_{ij} is the angle between the i and j ion spins. Taking into account that for the uncorrelated spins $\langle \cos \theta_{ij} \rangle = \langle \cos \theta_i \rangle^2 = (M/M_s)^2$, MR$(H) = \exp[-\alpha(M/M_s)^2]$, where $\alpha = E_A^0/k_B T$.

Let us first analyze the field-dependent MR of the low Sr-doped films. Because we assume that these films turn out to be in a paramagnetic state, the magnetization can be expressed by the Brillouin function $B_S(g\mu_B H/k_B T)$, where $g = 2$ is the Landé factor and μ_B is the Bohr magneton. The average spin for this composition is $S = \sqrt{0.3 S_1(S_1 + 1) + 0.7 S_2(S_2 + 1)} = 2.3076$, where $S_1 = 3/2$ and $S_2 = 2$ are the spin values of Mn^{4+} and Mn^{3+} ions, respectively. The prior analysis of the $R(T)$ dependence for $y = 0$ at $T \geq T_C, T_P$ allow us to estimate the field-independent activation energy as $E_A^0 = 1500$ K in the temperature units, and therefore, $\alpha = 5$ at $T = 300$ K. The inset in Fig. 6 displays the experimental (solid line) and both theoretical (dashed lines) MR(H) curves for $y = 0.3$. For the better agreement between theory and experimental data we used $S_{\text{eff}} = NS$ as the fitting parameter. Here S_{eff} is treated as an effective polaron spin which consists of N single ion ones [25]. It is seen that both the considered approaches with the same degree of accuracy describe MR(H) behavior for $y = 0.3$. Moreover, the exploitable fitting parameters are very close to each other, $N = 3.5$ and 2.35 for the Appel [30] and the field-dependent activation energy [25,31] models, respectively.

Unfortunately the MR(H) dependence for the $y = 0.9$ film can not be adequately described in the framework of DE model, which also predicts the parabolic MR(H) dependence instead of the near linear one, manifested by the experiment [29]. The main reason for that is probably the inhomogeneous (phase-separated) magnetic state of the high Sr-doped $(y \geq 0.65)$ films at room temperature. It is confirmed by the anhysteretic MR(H) behavior in a low-field range, which is contradicted with that for the similar films being in the completely FM state [32]. This hysteresis becomes apparent in the form of two splitted peaks located near a coercive field and is provided by the hysteretic behavior of magnetization loop for ferromagnet [33]. Therefore, one can conclude that our $y \geq 0.65$ films at room temperature represent the magnetic phase-separated system, containing the FM and paramagnetic (PM) clusters. As we discussed

before, the formation of this multiphase magnetic state also can be affected by a nonuniform distribution of the lattice strain. The description of a magnetoresistance for a such type of the magnetic phase-separated system can be understood in the framework of the approach presented by Wagner et al. [34]. According to this phenomenological model, the activation barrier (they consider the Mott hopping mechanism of conductivity [31], but it is not fundamental point in our case) includes two main field-affected terms. First of them is similar to considered above for the PM state and reveals $E_A \sim B_S^2(g\mu_B H/k_B T)$, while the second one (so-called the Weiss magnetization contribution) becomes dominant in the FM state and manifests a linear magnetic-field dependence of the activation energy $E_A \sim B_S(g\mu_B H/k_B)$. The experimental MR($H$) dependence for $y = 0.9$ (see the inset in Fig. 6) was approximated by an expression MR(H) = $= \exp[-\alpha(M/M_s)]$ with the number of the single-ion spins N as a fitting parameter and $\alpha = E_A^0/k_B T = 5$ again. It is seen that the theoretical curve is practically coincident with the experimental data at $N = 1.2$.

Therefore, the magnetotransport properties of the $La_{0.7}(Ca_{1-y}Sr_y)_{0.3}MnO_3$ films at room temperature can be excellently described within the framework of a field-affected activation energy approximation, taking into account a competition between the spin-dependent trapping of charges in PM state and the Weiss-magnetization contribution in FM one.

Conclusions

We have studied the magnetic and transport properties of $La_{0.7}(Ca_{1-y}Sr_y)_{0.3}MnO_3$ films as-deposited on $LaAlO_3$ (001) single crystal substrates. Microstructure analysis reveals that the films at $0.3 \leq y \leq 0.5$ are phase-separated into nanoscale clusters with the orthorhombic and rhombohedral crystal structure at room temperature. The observed clustering accompanied by the two-stage magnetic and electronic transition in the films. It was shown that for the $0.5 \geq y \geq 0$ films a nonlinear (almost parabolic) MR(H) dependence is typical, while for the $0.65 \leq y \leq 1.0$ films a linear MR(H) behavior is observed at 300 K. The magnetotransport properties of the $La_{0.7}(Ca_{1-y}Sr_y)_{0.3}MnO_3$ films at room temperature can be explained on the base of a field-dependent activation energy model, considering simultaneously the spin-dependent trapping of charges in PM state and the Weiss-magnetization contribution at the FM ordering. Using the experimental data, the magnetic phase diagram was constructed for the $La_{0.7}(Ca_{1-y}Sr_y)_{0.3}MnO_3$ thin-film system.

1. J. Volger, *Physica* (*Utrecht*) **20**, 49 (1954).
2. S. Chahara, T. Ohno, K. Kasai, and Y. Kozono, *Appl. Phys. Lett.* **63**, 1990 (1993).
3. R. von Helmolt, J. Wecker, B. Holzapfer, L. Schultz, and K. Samwer, *Phys. Rev. Lett.* **71**, 2331 (1993).
4. S. Jin, T.H. Tiefel, M. McCormack, R.A. Fastnacht, R. Ramesh, and L.H. Chen, *Science* **264**, 413 (1994).
5. For a Review, see *Collosal Magnetoresistance Oxides*, Y. Tokura (ed.), Gordon and Breach, London (1999).
6. C. Zener, *Phys. Rev.* **82**, 403 (1951).
7. P.W. Anderson and H. Hasegawa, *Phys. Rev.* **100**, 675 (1955).
8. P.-G. de Gennes, *Phys. Rev.* **118**, 141 (1960).
9. A.J. Millis, *Phys. Rev.* **B53**, 8434 (1996); A.J. Millis, R. Mueller, and B.I. Shraiman, *Phys. Rev.* **B54**, 5389 (1996); A.J. Millis, R. Mueller, and B.I. Shraiman, *Phys. Rev.* **B54**, 5405 (1996); A.J. Millis, B.I. Shraiman, and R. Mueller, *Phys. Rev. Lett.* **77**, 175 (1996).
10. J. Zang, A.R. Bishop, and H. Röder, *Phys. Rev.* **B53**, R8840 (1996).
11. For a Review, see E. Dagotto, T. Hotta, and A. Moreo, *Phys. Rep.* **344**, 1 (2001).
12. V. Kiryukhin, T.Y. Koo, H. Ishibashi, J.P. Hill, and S-W. Cheong, *Phys. Rev.* **B67**, 064421 (2003).
13. P.G. Radaelli, M. Morezio, H.Y. Hwang, S.-W. Cheong, and B. Batlogg, *Phys. Rev.* **B54**, 8992 (1996).
14. P.G. Radaelli, M. Morezio, H.Y. Hwang, and S.-W. Cheong, *J. Solid State Chem.* **122**, 444 (1996).
15. Y. Tomioka, A. Asamitsu, and Y. Tokura, *Phys. Rev.* **B63**, 024421 (2000).
16. A.N. Ulyanov, S.C. Yu, N.Yu. Starostyuk, N.E. Pismenova, Y.M. Moon, and K.W. Lee, *J. Appl. Phys.* **91**, 8900 (2002).
17. A.N. Ulyanov and S.C. Yu, *Physica* **B368**, 42 (2005).
18. V.G. Prokhorov, G.G. Kaminsky, V.A. Komashko, J.S. Park, and Y.P. Lee, *J. Appl. Phys.* **90**, 1055 (2001).
19. O.I. Lebedev, G. Van Tendeloo, S. Amelinckx, B. Leibold, and H.-U. Harbermeier, *Philos. Mag.* **A79**, 1561 (1999).
20. O.I. Lebedev, G. Van Tendeloo, S. Amelinckx, H.L. Ju, and K.M. Krishnan, *Philos. Mag.* **A80**, 673 (2000).
21. T.K. Nath, R.A. Rao, D. Lavric, C.B. Eom, L. Wu, and F. Tsui, *Appl. Phys. Lett.* **74**, 1615 (1999).
22. E. Snoeck, B. Warot, H. Ardhuin, A. Rocher, M.J. Casanove, R. Kilaas, and M. J. Hÿtch, *Thin Solid Films* **319**, 157 (1998).
23. H.Y. Hwang, S.W. Cheong, N.P. Ong, and B. Batlogg, *Phys. Rev. Lett.* **77**, 2041 (1996).
24. Y. Lyanda-Geller, S.H. Chun, M.B. Salamon, P.M. Goldbart, P.D. Han, Y. Tomioka, A. Asamitsu, and Y. Tokura, *Phys. Rev.* **B63**, 184426 (2001).
25. G. Jakob, W. Westerburg, F. Martin, and H. Adrian, *Phys. Rev.* **B58**, 14 966 (1998).
26. P.R. Broussard, S.B. Qadri, V.M. Browning, and V.C. Cestone, *J. Appl. Phys.* **85**, 6563 (1999).
27. M. Varma, *Phys. Rev.* **B54**, 7328 (1996).

28. M. Medarde, M. Mesot, P. Lacorre, S. Rosenkranz, P. Fisher, and K. Grobcht, *Phys. Rev.* **B52**, 9248 (1995).

29. N. Furukawa, *J. Phys. Soc. Jpn.* **64**, 2734 (1995); 2754 (1995).

30. J. Appel, *Phys. Rev.* **B141**, 506 (1966).

31. M. Viret, L. Ranno, and J.M.D. Coey, *Phys. Rev.* **B55**, 8067 (1997).

32. A. de Andés, S. Taboada, J.M. Colino, R. Ramirez, M. Garsia-Hernándes, and J.L. Martinez, *Appl. Phys. Lett.* **81**, 319 (2002).

33. G.J. Snyder, M.R. Beasley, T.H. Geballe, R. Hiskes, and S. DiCarolis, *Appl. Phys. Lett.* **69**, 4254 (1996).

34. P. Wagner, I. Gordon, L. Trappeniers, J. Vanacken, F. Herlach, V.V. Moshchalkov, and Y. Bruynseraede, *Phys. Rev. Lett.* **81**, 3980 (1998).